

EXAFS Studies on the Size Dependence of Structural and Dynamic Properties of CdS Nanoparticles

Jörg Rockenberger,[†] Larc Tröger,^{*,‡} Andreas Kornowski,[†] Tobias Vossmeier,[§]
Alexander Eychmüller,[†] Josef Feldhaus,[‡] and Horst Weller^{*,†}

*Institut für Physikalische Chemie, Universität Hamburg, Bundesstrasse 45, D-20146 Hamburg, Germany, and
Hamburger Synchrotronstrahlungslabor HASYLAB at Deutsches Elektronen-Synchrotron DESY,
Notkestrasse 85, D-22603 Hamburg, Germany*

Received: October 21, 1996; In Final Form: January 2, 1997[®]

Size-dependent structural and dynamic properties of CdS nanocrystals with 13–120 Å diameter and of molecular crystals consisting of three-dimensional superlattices of these nanoparticles have been determined by extended X-ray absorption fine structure spectroscopy (EXAFS) at the Cd K edge at temperatures between 5 and 290 K. It is shown that these properties are governed by the surface-to-volume ratio and the way of surface stabilization of the nanoparticles. Thiol-capped CdS nanoparticles with diameters from 13 to 40 Å show an expansion of the mean Cd–S distance whereas mean interatomic distances in polyphosphate-stabilized particles with 30–120 Å diameter are slightly contracted with respect to CdS bulk. By measuring the EXAFS spectra between 5 and 290 K, the total mean-square relative displacement could be separated into a static part which is independent of temperature and into a dynamic temperature-dependent part. The temperature-independent mean-square relative displacement (or static disorder) of the Cd–S bonds exhibits a maximum at cluster sizes of about 30 Å separating thermodynamically and kinetically controlled growth regimes. Vibrational amplitudes of the Cd–S bonds are only very slightly damped with decreasing particle size. Careful investigations of the asymmetry of the interatomic Cd–S pair potential indicate the possibility to distinguish between CdS nanoparticles with zinc blende and wurtzite structure in cases where alternative methods such as powder X-ray diffraction or transmission electron microscopy fail.

1. Introduction

Nanocrystalline materials provide very interesting substances for material science since their properties deviate from the respective bulk material in a size-dependent manner.^{1–3} Especially, in semiconductor nanoparticles the blue shift of their UV–vis absorption maxima with decreasing particle diameter can be easily observed and understood from the size quantization effect.⁴ With suitable chemical preparation routes it should be possible to tune a specific property such as the electronic band gap, magnetization, heat capacity, and others of a nanoparticle to a specific problem.

Despite the fact that a size dependence of physical properties of nanoparticles has been observed in many systems, less is known about the structural properties of these nanoparticles. One reason is that only in a few cases has one succeeded in crystallizing clusters in three-dimensional superlattices to study their structural properties by single-crystal X-ray diffraction (SC-XRD). Prominent examples for macroscopic crystalline materials consisting of semiconducting nanocrystals arranged in three-dimensional superlattices (in the following referred to as molecular crystals of CdS nanoparticles) are [Cd₁₇S₄(SPh)₂₈]-[N(CH₃)₄]₂ by Lee et al.,⁵ Cd₃₂S₁₄(SPh)₃₆·4DMF by Herron et al.,⁶ and Cd₁₇S₄(SCH₂CH₂OH)₂₆ and Cd₃₂S₁₄(SCH₂CH(OH)-CH₃)₃₆·4H₂O by Vossmeier et al.^{7,8} Remarkably, in all four cases the structure of the cluster unit determined by SC-XRD is a tetrahedral cutout of the CdS zinc blende bulk lattice whose surface is stabilized by the thiol ligands. However, the three-

dimensional arrangement of the nanoclusters differs extraordinarily in these crystals. For example, the crystal structure of Cd₁₇S₄(SCH₂CH₂OH)₂₆ consists of tetrahedral Cd₁₇S₃₀-cluster cores which are covalently linked at the four edges by a (μ_2 -S)-bridging thiol to form a superlattice. In this superlattice, individual clusters are arranged like atoms in the zinc blende structure. The Cd₃₂S₁₄(SCH₂CH(OH)CH₃)₃₆·4H₂O cluster is a larger structure homologue of the Cd₁₇S₃₀ cluster with one more CdS plane at the basis of the tetrahedron, and its edges are terminated by water molecules. The superlattice of this cluster unit is described by a van der Waals lattice with a double layer structure.

Apart from these few examples there exist a lot of nanocrystalline substances which appear amorphous in X-ray diffraction measurements but where the individual nanoparticles are crystalline on a nanometer scale. For example, a series of 1-thioglycerol-stabilized nanocrystalline CdS particles has been synthesized and characterized over a wide size range.⁹ With regard to UV–vis absorption and particle diameter the smallest clusters of this series which cannot be isolated as single crystals are equivalent to the already mentioned molecular crystals of CdS nanoparticles. More recently, very well ordered colloidal crystals and films of almost monodisperse CdSe nanoparticles with diameters between 15 and 100 Å could be synthesized by Bawendi and co-workers.¹⁰

To obtain structural information on nanoparticles in such samples the measurement of the extended X-ray absorption fine structure (EXAFS) is very well suited since this method in contrast to SC-XRD does not rely on any long-range order in the sample. Also, EXAFS is not limited to only the solid state but can also be measured on liquid systems or even in cluster beams in the gas phase,¹¹ enabling the identification of inter-cluster interactions by comparison to solid state measurements.

* Corresponding authors.

[†] Universität Hamburg.

[‡] DESY.

[§] Present address: Department of Chemistry and Biochemistry, University of California, Los Angeles, 405 Hilgard Avenue, Los Angeles, CA 90095.

[®] Abstract published in *Advance ACS Abstracts*, March 1, 1997.

TABLE 1: List of the Prepared and Investigated CdS Nanoparticles^a

sample	ligand ^b	morphology	λ (nm)	particle diameter (Å) from		SC-XRD	TEM	mean particle diameter (Å)
				powder X-ray diffraction				
				$2^\circ \leq 2\Theta \leq 10^\circ$ ^c	$20^\circ \leq 2\Theta \leq 60^\circ$ ^d			
1	TG	crystals	242	13.2		13.2 ^e		13.2
2	TE	crystals	292	13.5		13.1 ^f		13.3
3	TiP	crystals	323	17.0		17.9 ^f		17.5
4	TG	powder	294	14.2				14.2
5	TG	powder	333	18.5				18.5
6	TG	powder	366	23.1				23.1
7	TG	powder	407	38.0	42.2			40.1
8	PP	powder	450		28.1 ^g			28.1
9	PP	powder	475		52.4		58.0 ^h	55.2
10	PP	powder	490		107.0		137.6 ^h	122.3
11		powder	515					∞

^a The onset of the UV-vis absorption has been determined from the minimum of the second derivative of the spectra. Powder X-ray diffraction in the small- and wide-angle regime, single crystal X-ray diffraction, and transmission electron microscopy have been used to determine particle diameters. ^b TG, 1-thio-2,3-propanediol; TE, 1-thio-2-ethanol; TiP, 1-thio-2-propanol; PP, polyphosphate. ^c Using the Bragg equation for the particle interference peak. ^d Using the Debye-Scherrer formula with $K = 1$ and taking the mean over all reflections. ^e Diameter of a cylinder incorporating a $\text{Cd}_8(\text{thioglycerol})_{16}$ unit. ^f Calculated as a sphere with radius from the clusters center to a Cd atom at the corner of the tetrahedron. ^g As known from TEM, samples with similar absorption spectra yield particles with 40 Å diameter. ^h Standard deviation in size is 24 and 29%, respectively.

Consequently, a lot of EXAFS work has already been done to get structural information on nanoparticles. For example, the $\text{Au}_{55}(\text{PPh}_3)_{12}\text{Cl}_6$ cluster and similarly stabilized Pd clusters of higher nuclearity prepared by Schmidt et al.^{12–14} have been investigated by EXAFS.^{15–17} EXAFS measurements on semi-conducting systems have been performed on CdSe clusters prepared in zeolites at the Cd and Se K edge,¹⁸ thiophenol- and selenophenol-stabilized CdSe and CdS clusters at the Se K edge,¹⁹ and CdX (X = S, Se, Te) nanoparticles at the Cd, Se, and Te K edge.²⁰ Recently, CdS nanoparticles in dimethylformamide solutions have also been characterized by EXAFS at the Cd K edge.²¹ Of course, EXAFS is also an important tool to study small supported particles in the field of catalysis.^{22–24}

In this study, we measured the EXAFS at the Cd K edge of a series of very well characterized CdS nanoparticles listed in Table 1 over the wide size range of 13–120 Å in diameter. By varying the ligand type within this cluster series, we are sensitive to structural changes induced by the interaction between the ligand and the Cd atoms at the surface of the nanoparticles. To separate static bond length variations and temperature-dependent dynamics within these particles, temperature-dependent EXAFS measurements have been performed between 5 and 290 K. Furthermore, the existence of molecular crystals of CdS nanoparticles with known structure from SC-XRD allows the direct comparison of EXAFS and SC-XRD results with respect to interatomic distances and mean coordination numbers, for instance. In a first attempt to identify an influence of intercluster interactions on the structure of the nanoparticle, an aqueous solution of the $\text{Cd}_{32}\text{S}_{14}(\text{SCH}_2\text{CH}(\text{OH})\text{CH}_3)_{36}\cdot 4\text{H}_2\text{O}$ clusters has also been measured at 290 K.

2. Experimental Section

The investigated samples can be divided into three groups (see Table 1). First, samples 1–3 can be obtained as molecular crystals and their crystal structure can be determined by SC-XRD. Samples 2 and 3 are the already mentioned crystalline $\text{Cd}_{17}\text{S}_4(\text{SCH}_2\text{CH}_2\text{OH})_{26}$ and $\text{Cd}_{32}\text{S}_{14}(\text{SCH}_2\text{CH}(\text{OH})\text{CH}_3)_{36}\cdot 4\text{H}_2\text{O}$ clusters. Furthermore, the crystalline cadmium 1-thioglycolate, $\text{Cd}(\text{SCH}_2\text{CH}(\text{OH})\text{CH}_2\text{OH})_2$ (sample 1), has been investigated since its structure consists of a three-dimensional network of $\text{Cd}_8(\text{SCH}_2\text{CH}(\text{OH})\text{CH}_2\text{OH})_{16}$ units which resemble the surface of the $\text{Cd}_{17}\text{S}_4(\text{SCH}_2\text{CH}_2\text{OH})_{26}$ and $\text{Cd}_{32}\text{S}_{14}(\text{SCH}_2\text{CH}(\text{OH})\text{CH}_3)_{36}\cdot 4\text{H}_2\text{O}$ clusters.²⁵ This sample is thought to be a reference in addition to the investigated CdS bulk (sample 11)

to separate contributions of the surface and the interior of the nanoparticles to the measured EXAFS spectra.

The second group consists of nanocrystalline CdS particles with 1-thioglycerol as stabilizing ligand and diameters from 14 to 40 Å (samples 4–7). In order to identify the influence of the surface stabilization through differing ligands on the structure, polyphosphate-stabilized CdS nanoparticles with 30–120 Å diameter (samples 8–10) were investigated as the third group.

2.1. Preparation and Characterization. Crystalline samples 1–3 have been prepared following the description in literature.^{7,8,25} Briefly, $\text{Cd}(\text{SCH}_2\text{CH}(\text{OH})\text{CH}_2\text{OH})_2$ (sample 1) was prepared by slowly decreasing the pH value of an alkaline aqueous solution of $\text{Cd}(\text{ClO}_4)_2\cdot 6\text{H}_2\text{O}$ and 1-thioglycerol by dialyzation against deionized water. A similar procedure has been used to prepare crystals of the $\text{Cd}_{17}\text{S}_4(\text{SCH}_2\text{CH}_2\text{OH})_{26}$ and $\text{Cd}_{32}\text{S}_{14}(\text{SCH}_2\text{CH}(\text{OH})\text{CH}_3)_{36}\cdot 4\text{H}_2\text{O}$ nanoparticles (samples 2 and 3). Here, different amounts of H_2S were added to the alkaline aqueous solutions of $\text{Cd}(\text{ClO}_4)_2\cdot 6\text{H}_2\text{O}$ and thiol ligands, 1-thioethanol and 1-thio-2-propanol, respectively. By dialyzing against deionized water, small colorless crystals grew while the pH value of the solution decreased.

The synthesis and characterization of nanocrystalline, 1-thioglycerol-capped CdS clusters (samples 4–7) is described in detail in ref 9. Samples 4 and 5 were prepared by adding different amounts of 1-thioglycerol and H_2S to a solution of $\text{Cd}(\text{ClO}_4)_2\cdot 6\text{H}_2\text{O}$ in water and different subsequent heat treatment. To prepare samples 6 and 7 a solution of cadmium acetate in dimethylformamide with thiourea as sulfur source was refluxed. Only 0.475 g (6.42 mmol) of thiourea has to be added to 2.35 g (8.82 mmol) of $\text{Cd}(\text{CH}_3\text{COO})_2\cdot 2\text{H}_2\text{O}$ and 0.95 mL of (10.95 mmol) 1-thioglycerol in 200 mL of dimethylformamide, which is just half the amount published in ref 9. After a short dialyzation, in both cases the crude products were separated and cleaned by size-selective precipitation.²⁶ The polyphosphate-stabilized CdS nanoparticles (samples 8–10) were synthesized following well-established procedures.²⁷

In all cases preparation and quality of the dissolved products were controlled by measuring the UV-vis absorption (Perkin-Elmer Lambda 14) which serves as a simple fingerprint to monitor the size and size distribution of the prepared nanoclusters. Further, the dried and powdered samples were characterized by powder X-ray diffraction (Philips X'pert, Cu K α radiation, variable entrance slit, Bragg-Brentano geometry,

secondary monochromator) to determine particle diameter and the lattice structure of the nanoparticles. The diameter of the larger polyphosphate-stabilized nanoparticles was also determined by transmission electron microscopy (Philips CM12).

All samples were washed with ether to remove water, dried in vacuum, and powdered. For the EXAFS measurements the powders were mixed with boron nitride, homogenized by extensive grinding, and pressed to form stable pellets. Care was taken that the applied pressure was more than a magnitude below a point where phase transitions in nanoparticles are known to occur.^{28,29}

2.2. Extended X-ray Absorption Fine Structure. Temperature-dependent EXAFS measurements between 5 and 290 K at the Cd K edge have been performed at beamline X1.1 of the DORIS storage ring at HASYLAB, DESY (Hamburg, Germany). This beamline is equipped with a Si(311) double-crystal monochromator which was detuned to 60% of the Bragg peak intensity to eliminate higher harmonics. EXAFS data of a sample and simultaneously of Cd metal foil (Goodfellow) as reference were measured between 26.4 and 29.0 keV in transmission with three ionization chambers. The temperature of the sample was varied between 5 and 290 K by a liquid He bath cryostat (Oxford). The amount of sample in each pellet was chosen to give an absorption of about $\mu d = 1.5$ at the Cd K edge. In the case of sample 3 less material was available, which causes a worse signal-to-noise ratio in these spectra.

To make sure that irradiation effects of the synchrotron radiation on the samples are weak, two powdered samples of $\text{Cd}_{17}\text{S}_4(\text{SCH}_2\text{CH}_2\text{OH})_{26}$ were irradiated in air at room temperature for 30 and 90 min with photon energies above the Cd K edge (26800 eV) at a photon flux of about 5×10^8 photons/(s mm²). Characterization of these samples included UV-vis absorption, powder X-ray diffraction, and Rietveld analysis of the powder diffraction pattern based on the structure data from SC-XRD. As already observed in earlier studies⁷ the samples exhibit a certain radiation sensitivity since the superlattice reflections monitored by powder X-ray diffraction decrease after elongated X-ray exposure. Therefore, care was taken to limit EXAFS scanning times to values where no radiation-induced decomposition is observed. It was further checked that the UV-vis spectra of freshly prepared and irradiated cluster samples were identical.

For data analysis the usual procedures of background subtraction, normalization, and transfer to k -space were performed.³⁰ The position of the Cd K absorption edge determined from the maxima of the first derivative is for all samples within ± 0.5 eV identical to the one of the simultaneously measured Cd metal. Therefore, the absorption edge shift ΔE_0 was determined by fitting the EXAFS spectra of CdS bulk (sample 11) at 5 K with ΔE_0 as variable. For all other samples and temperatures ΔE_0 was set constant to this fitted value. The background-subtracted data were k^3 weighted and Fourier transformed between $k = 3.5$ and 16.0 \AA^{-1} . The FEFFIT package Ver. 2.32³¹ was used to fit the data in real space with the help of theoretical backscattering amplitudes and phases which were calculated with the FEFF code Ver. 5.³² The Cd-S and the Cd-Cd coordination were fitted individually using single-scattering paths since the amplitude of multiscattering contributions is below 10%. It was checked that the fitting results of the individual shells do not change when both shells are fitted at the same time.

Fitting of the Cd-S coordination shell was done in real space between $r = 1.5$ and 2.5 \AA with a mean Cd-S interatomic distance $R_{\text{Cd-S}}$, a mean-square relative displacement (MSRD) σ^2 , and an anharmonicity parameter C_3 as variables. It might

be expected that in small clusters a splitting of the Cd-S shell corresponding to a surface and cluster core contribution becomes effective. Attempts to employ this concept into two-shell fits of the first peak in the Fourier transform of the EXAFS function do not support this idea. This can be understood by closer inspection of the intracluster Cd-S bond length distribution obtained by SC-XRD of the smallest crystalline samples 2 and 3: no systematic enlargement of Cd-S distances located at the cluster surface with respect to Cd-S bonds in the cluster core is observed (see also section 4).

The Cd-S coordination number was set to $N_{\text{Cd-S}} = 4$ because as known from SC-XRD all Cd atoms are 4-fold coordinated by sulfur in samples 1–3. This assumption could be seen as arbitrary in case of the polyphosphate-stabilized samples 8–10 since there is no experimental evidence for these large particles that every Cd atom at the surface is 4-fold coordinated by sulfur. Therefore, we checked this assumption by fitting the Cd-S shell and additionally varying the coordination number in all samples. The results showed no size-dependent variation of the coordination number and were identical to the expected value of 4 within the error bars of 10%. Additionally, in the case of the polyphosphate-stabilized nanoparticles (samples 8–10) it was checked that a possible oxygen coordination at the surface does not contribute significantly to the first coordination shell of the Cd atom.

In contrast, the Cd-Cd coordination at 5 K was fitted between 3.4 and 4.2 \AA by varying a mean Cd-Cd interatomic distance $R_{\text{Cd-Cd}}$, a MSRD σ^2 , an anharmonicity parameter C_3 , and the coordination number $N_{\text{Cd-Cd}}$ because here a strong size-dependent variation is to be expected. For all other temperatures the coordination number was fixed to the fitting result at 5 K and only mean distances, the MSRDs, and the anharmonicity parameters were fitted. Inclusion of weaker single- and multiple-scattering paths was checked and observed to be negligible.

We used the multi-file-fit option in the FEFFIT package to fit all spectra of one sample at different temperatures at the same time. By using the implemented correlated Debye model which gives a relation between the dynamic MSRD σ_{dyn}^2 and the Debye temperature T_D , we fitted the total MSRD σ_{tot}^2 as the sum of a temperature-independent part σ_{stat}^2 which reflects a static bond length distribution (static disorder) and a temperature-dependent part σ_{dyn}^2 which is described by T_D as the only parameter. Therefore, the variables in these multi-file fits were mean distances and anharmonicity parameters at the different temperatures, the static MSRD σ_{stat}^2 and the Debye temperature. As in the case of individual fits, the coordination numbers were set to $N_{\text{Cd-S}} = 4$ and $N_{\text{Cd-Cd}} = N_{\text{Cd-Cd}}(5 \text{ K})$, respectively. It should be noticed that using the multi-file-fit option couples the dynamic MSRDs at different temperatures, thereby reducing the total number of fitting parameters and increasing the reliability of the fit parameters with respect to a number of single-file fits (e.g., for fitting of typically five spectra from 15 to 12). It was observed that results of single-file fits are consistent within their error bars with multi-file fits.

3. Results

3.1. Characterization. UV-Vis Spectra. In Figure 1 the UV-vis absorption spectra of solutions of samples 2–10 are shown. It is clearly seen that with decreasing particle diameter the absorption maximum shifts to shorter wavelengths due to the increasing confinement of the photogenerated charge carriers in small particles. Also, the absorption spectra become more structured with decreasing size because the electronic band structure changes to molecular levels with nonvanishing energy spacing.

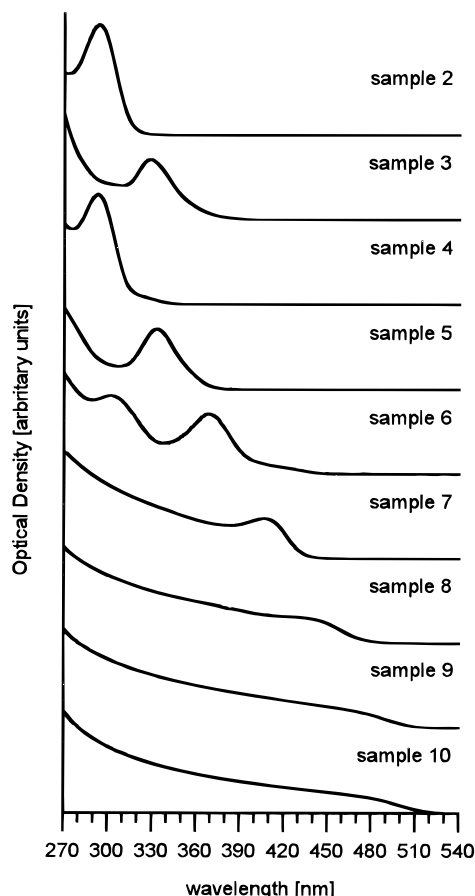


Figure 1. UV-vis absorption spectra of solutions of samples 2–10 in water or dimethylformamide. Note the shift of the absorption onset to shorter wavelengths with decreasing particle diameters.

Powder X-ray Diffraction. The Rietveld analysis of the powder diffraction pattern of powdered $\text{Cd}_{17}\text{S}_4(\text{SCH}_2\text{CH}_2\text{OH})_{26}$ crystals using the DBWS package of Young et al.³³ showed a slight decrease of the lattice constants a , b , and c and of the monoclinic angle β with respect to the results of the SC-XRD which was performed on crystals in mother liquor. After exposure to synchrotron radiation no significant changes in the UV-vis absorption and in the powder X-ray diffraction patterns were observed.

The diameter of the CdS nanoparticles 1–7 was determined by means of powder X-ray diffraction in the small-angle regime. In Figure 2 (left) the respective diffraction patterns of samples 4–7 are shown in the range of $2^\circ \leq 2\Theta \leq 10^\circ$. Sharp diffraction peaks are observed for samples 4–6, whereas sample 7 shows just a shoulder. To identify the diffraction peak in sample 7, the profile has been fitted by a sum of a pseudo-Voigt function and an exponential decay of the primary intensity. Assuming a local densest packing of the CdS nanocrystals, this diffraction peak can be correlated in first order with lattice planes through the cluster's center of mass. Using the Bragg equation, the respective lattice plane spacing acts as an estimate of the cluster diameter including the ligand shell. Resulting particle diameters are listed in Table 1 together with results of other size determination methods. For samples 1–3, a good agreement exists between diameters determined by this method and the result of the SC-XRD. In the case of sample 6 a second peak in the small-angle regime at the double angle of the first diffraction peak can clearly be observed. This is interpreted as a higher-order superlattice reflection indicating the very high intercluster ordering in this sample. Samples 8–10 show no particle interference peak in the given angle regime. For samples 9 and 10 this is expected since the respective diffraction

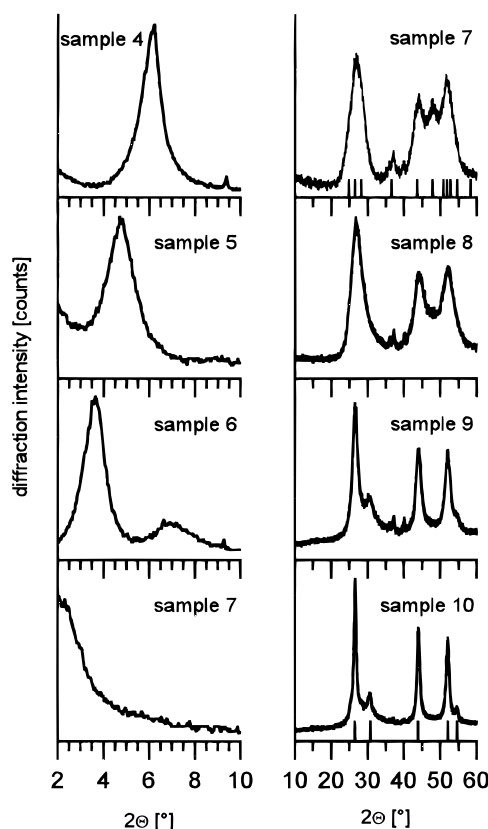


Figure 2. Powder X-ray diffraction patterns of samples 4–10. Particle diameters were obtained for samples 4–7 from the small-angle regime by analyzing the position of the diffraction peak via the Bragg equation. For samples 7–10, the peak broadening due to the finite crystal size was used to determine the particle diameters. The small bars in the diffraction patterns at the bottom and the top indicate the positions of diffraction peaks in cubic and hexagonal CdS bulk, respectively.

peak lies below $2\Theta = 2.0^\circ$. In the case of sample 8 a particle diameter of 28 Å was determined from the peak broadening by the Debye–Scherrer equation in the wide-angle diffraction regime which should give a particle interference peak at $2\Theta = 3.2^\circ$. For several reasons discussed below the particle diameter in this sample is likely to be underestimated by analyzing the peak broadening.

Because of their very broad diffraction patterns in the wide-angle X-ray diffraction regime, no information about the lattice structure can be obtained for the small nanoclusters in samples 4–6. On the other hand, diffraction patterns of samples 7–10 in Figure 2 (right) allow the determination of their crystalline structure. The polyphosphate-stabilized samples 8–10 show mainly a diffraction pattern of the zinc blende structure which is broadened due to the finite crystal size. On the other hand, sample 7 seems to consist mainly of a wurtzite phase: in Figure 2 the small bars in the upper and lower diffraction patterns indicate the peak positions of hexagonal and cubic CdS.³⁴ In the diffraction patterns of samples 4–10 small peaks at $2\Theta = 36.0^\circ$, 37.1° , and 40.0° can be seen which cannot be associated with a cubic or hexagonal CdS structure. Therefore, it must be concluded that a slight contamination is present in these samples. It was checked that these diffraction peaks do not correspond to Cd compounds like $\text{Cd}(\text{ClO}_4)_2 \cdot x\text{H}_2\text{O}$, CdO , $\text{Cd}(\text{OH})_2$, CdCl_2 , $\text{Cd}(\text{HCO}_3)_2$, and CdCO_3 .

Fitting the peaks of samples 7–10 with pseudo-Voigt functions located at positions of hexagonal and cubic CdS, respectively, and using the simplified Debye–Scherrer equation with a form factor of $K = 1$ gives an estimated particle diameter perpendicular to the reflecting lattice planes. For simplicity,

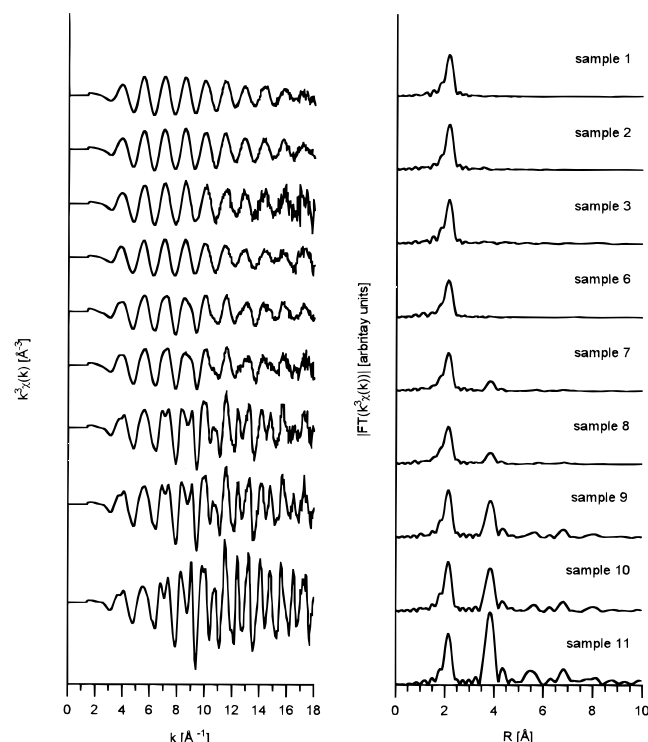


Figure 3. EXAFS functions $k^3\chi(k)$ and corresponding Fourier transforms at 5 K for samples 1–3 and samples 6–11. The spectra of samples 4 and 5 are practically identical to the results of the crystalline samples 2 and 3.

the particle diameters were determined in this manner and the mean values of the different (hkl) reflections are listed in Table 1.

Electron Microscopy. The diameter of the polyphosphate-stabilized particles of samples 9 and 10 were also determined by transmission electron microscopy images. For both samples the diameters of approximately 200 distinct particles have been measured and the mean diameter together with the standard deviation of the size distribution is listed in Table 1.

3.2. Extended X-ray Absorption Fine Structure. In Figure 3, the normalized, k^3 -weighted EXAFS data $k^3\chi(k)$ and the magnitude of their Fourier transforms of samples 1–3 and 6–11 at 5 K are displayed. In the Fourier transforms, the first strong peak around 2.1 \AA (not phase-corrected) corresponds to the Cd–S coordination which in all samples is quite similar in height and position. In contrast, the intensity of the Cd–Cd coordination peak around 3.9 \AA (not phase-corrected) decreases strongly with decreasing particle diameter and vanishes for samples 1–6. For the larger samples 9–11 still higher Cd coordination shells can be observed which correspond to respective shells in hexagonal CdS bulk (sample 11). In Figure 4 the magnitudes of the Fourier transforms of $k^3\chi(k)$ at different temperatures are shown for sample 2 (crystalline $\text{Cd}_{17}\text{S}_4(\text{SCH}_2\text{CH}_2\text{OH})_{26}$), sample 7 (1-thioglycerol-stabilized 40 \AA CdS nanoparticles), and sample 11 (CdS bulk). In all three samples, the temperature dependence of the intensity of the Cd–S coordination peak shows a very similar decrease of about one-third in height between 5 and 290 K. In contrast, the Cd–Cd coordination peak decreases strongly with increasing temperature and, even in the case of CdS bulk, it is not visible at room temperature. From Figure 4, it is seen directly that measurements of nanoparticles performed at liquid nitrogen temperature are not sufficient to determine all the EXAFS information, e.g., on static bond distance variations. Even at 50 K, higher shells are still considerably damped with respect to 5 K measurements.

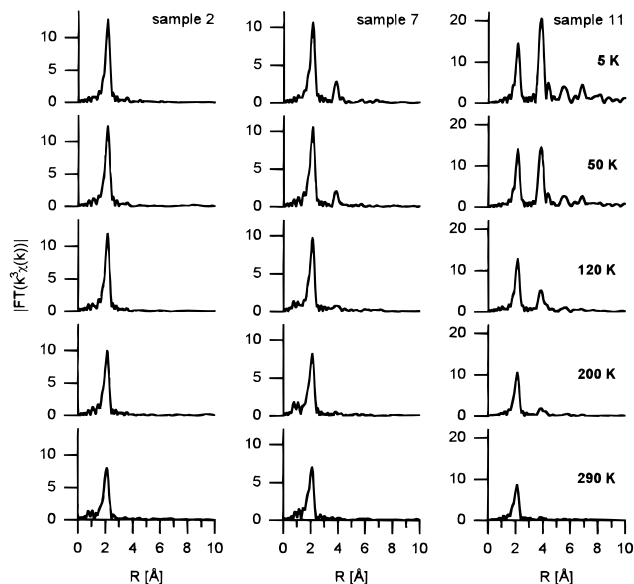


Figure 4. Fourier transforms of the EXAFS $k^3\chi(k)$ of the crystalline cluster $\text{Cd}_{17}\text{S}_4(\text{SCH}_2\text{CH}_2\text{OH})_{26}$ (sample 2), 40 \AA CdS nanoparticles (sample 7), and CdS bulk (sample 11) at five different temperatures.

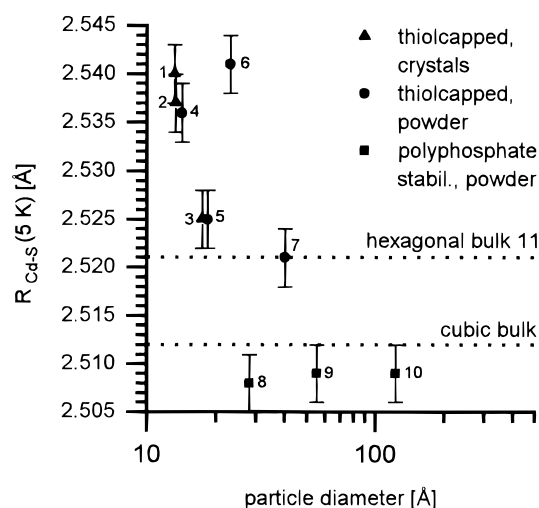


Figure 5. Mean Cd–S distance $R_{\text{Cd–S}}$ determined by EXAFS at 5 K as a function of the particle diameter. The values of hexagonal and cubic CdS bulk are indicated as dotted lines.

In the following, the results for the Cd–S and the Cd–Cd coordination will be presented separately.

Cd–S Coordination. Since we try to compare results determined by EXAFS and SC-XRD, absolute EXAFS distances must be of very high accuracy. The accuracy of EXAFS with respect to absolute distance determinations is limited by the precision of the used (theoretical) backscattering phase.^{35,36} However, due to the large available EXAFS data range in our study, relative changes in mean Cd–S distances between various samples could be determined within ± 0.003 \AA by employing identical analysis routines for all measured spectra. This allows us to observe clear size-dependent mean distance shifts in the cluster samples with respect to CdS bulk. In Figure 5, the mean Cd–S distances measured by EXAFS at 5 K are shown as a function of particle diameter. The absolute distance scale of Figure 5 is obtained by scaling the relative distance changes observed by EXAFS to the Cd–S bond length determined by powder X-ray diffraction on a pressed sample of hexagonal CdS bulk (sample 11) which was also measured as an EXAFS reference sample (upper dashed line in Figure 5).³⁷ Assuming an identical influence of pressure and temperature on cubic CdS

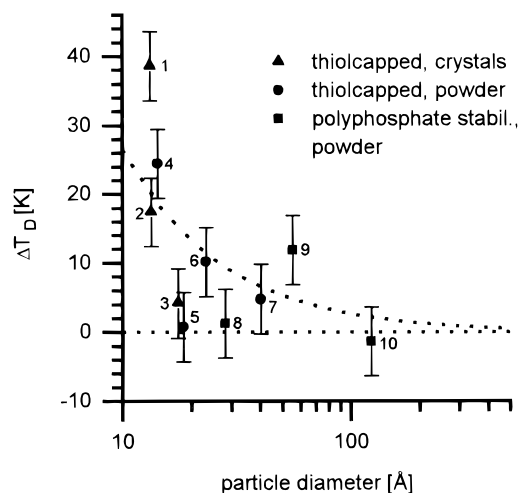


Figure 6. Shift of the Debye temperature ΔT_D of the Cd-S bonds as a function of particle diameter with respect to the result of CdS bulk. The Debye temperature of the first coordination shell in CdS bulk determined by EXAFS is 461 K. The dotted line is a fit of ΔT_D according to the surface-to-volume ratio of the particles.

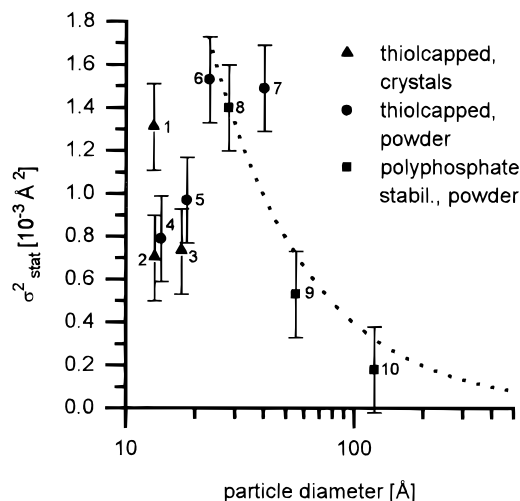


Figure 7. Static MSRD σ^2_{stat} of the Cd-S bonds as a function of particle diameter with respect to the result of CdS bulk. For the larger nanoparticles the observed increase with decreasing particle diameter can be described by their surface-to-volume ratio.

bulk, the lower dashed line in Figure 5 shows the Cd-S bond length in cubic CdS bulk at 5 K.³⁸

From Figure 5 it is obvious that the thiol- and polyphosphate-stabilized samples show different behavior. Thiol-capped samples (1–7) show an increasing expansion of their mean Cd-S distance with respect to hexagonal and cubic CdS bulk with decreasing particle diameter. In contrast, the polyphosphate-stabilized samples (8–10) show a decreased mean Cd-S distance with respect to cubic CdS bulk and only a slight size-dependent contraction. One further remarkable result is the very good agreement between the crystalline samples 2 and 3 and their respective nanocrystalline 1-thioglycerol-stabilized samples 4 and 5 with similar absorption maxima and particle diameters. This result supports the idea that in samples 4 and 5 the same cluster units as in the crystalline samples 2 and 3 are present but that their 1-thioglycerol ligands prevent crystallization into three-dimensional superlattices.

In Figures 6–8, the change of the Debye temperature, the static MSRD, and the third moment of the Cd-S pair distribution function obtained from the EXAFS data analysis are plotted as a function of particle diameter. Again, good agreement for

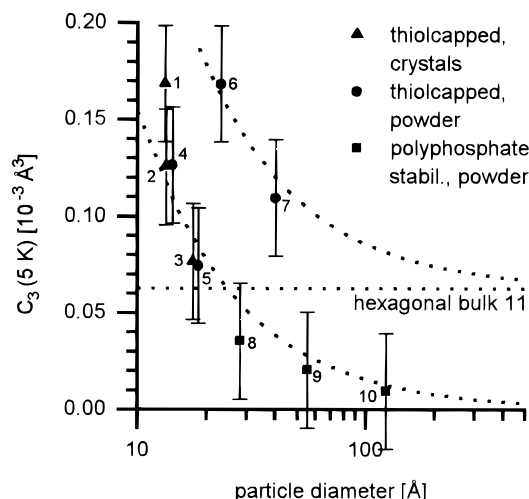


Figure 8. Third moment of the Cd-S pair distribution function C_3 at 5 K as a function of particle diameter. The experimental result of hexagonal CdS bulk is indicated as a horizontal, dotted line. Two different series each following the surface-to-volume ratio can be identified. They are assigned to the more asymmetric arrangement of neighboring atoms in hexagonal CdS (upper curve) and a more symmetric arrangement in cubic CdS (lower curve), respectively.

the results of the crystalline samples 2 and 3 and the 1-thioglycerol samples 4 and 5 can be seen.

The Debye temperature of the Cd-S bond in CdS bulk (sample 11) determined by EXAFS is $T_D = 461(3)$ K. As seen in Figure 6, changes in the Cd-S Debye temperatures of the cluster samples 2–10 are below 5% of this value. A slight increase in the Debye temperature with decreasing cluster size is observed, which corresponds to a stiffening of the CdS bonds. The overall trend of the observed shift can be described by the surface-to-volume ratio, i.e., a function $\Delta T_D = a/d$, where a is a fitting parameter and d the particle diameter (dotted line in Figure 6).

In all samples, the static MSRD σ^2_{stat} displayed in Figure 7 is increased with respect to CdS bulk. Decreasing the particle diameter from bulk, the static MSRD monotonically increases up to sizes between 20 and 40 Å. This trend also follows the increase of the surface-to-volume ratio. In contrast, smaller cluster samples (2–5) show a considerably reduced static MSRD with respect to nanoparticles of intermediate particle diameter.

The third moment C_3 of the Cd-S pair distribution function which reflects the anharmonicity of the pair potential is plotted in Figure 8. Two different groups with different absolute values of C_3 but a similar size dependence can be observed and very well described by the surface-to-volume ratio of the particles. As determined by powder or single-crystal X-ray diffraction, all particles with the smaller C_3 values have at least a cutout of a cubic CdS bulk lattice. In contrast, according to its powder X-ray diffraction pattern sample 7 seems to have mainly a hexagonal lattice whereas no decision can be made for sample 6. These two samples along with the EXAFS result of the hexagonal CdS bulk which is indicated in Figure 8 as horizontal dotted line show an enlarged C_3 value with respect to the cubic samples. Assuming that in the case of a cubic structure the anharmonicity of the interatomic pair potential is lower than in a hexagonal arrangement, Figure 8 suggests that the nanoparticles in sample 6 should also have a hexagonal lattice. The observed different anharmonicity for hexagonal and cubic lattices can be explained by the more symmetric arrangement of atoms in the cubic lattice which corresponds to a reduced anharmonicity of the interatomic pair potential (see section 4).

The fitting results of the EXAFS measurements of an aqueous solution of sample 3 at 290 K were practically identical to the

TABLE 2: EXAFS Fitting Results for the Cd–Cd Shell in Samples 7–11^a

sample	size	$N_{\text{Cd–Cd}}$ (5 K)	$R_{\text{Cd–Cd}}$ (5 K) (Å)	σ_{stat}^2 (10^{-3} Å^2)	C_3 (5 K) (10^{-3} Å^3)
7	40.1	3.3	4.126	2.2	0.33
8	28.1	3.5	4.111	1.4	0.29
9	55.2	7.7	4.104	−0.1	0.16
10	122.3	8.4	4.104	−0.3	0.18
11	∞	12.0	4.116	0.2	0.24

^a The expected error in the coordination number is $\pm 10\%$, in mean Cd–Cd distance $\pm 0.005 \text{ Å}$, in the static MSRD $\pm 0.5 \times 10^{-3} \text{ Å}^2$, and in the anharmonicity parameter $C_3 \pm 0.3 \times 10^{-3} \text{ Å}^3$.

results of the pressed powder pellets at the same temperature. The mean Cd–S distance in the dissolved nanoparticles is identical within 0.01 Å whereas the total MSRD shows no change within the error bars with respect to the solid state measurements. This result indicates that even in the dissolved state these nanoparticles have an enlarged mean Cd–S distance with respect to cubic CdS bulk.

Cd–Cd Coordination. The Cd–Cd coordination shell at different temperatures has been fitted by varying the mean distance $R_{\text{Cd–Cd}}$, the Debye temperature T_D , and the static MSRD σ_{stat}^2 using a coordination number $N_{\text{Cd–Cd}} = N_{\text{Cd–Cd}}(5 \text{ K})$ as constant parameter. $N_{\text{Cd–Cd}}(5 \text{ K})$ was determined in a single-file fit at 5 K. The results of the fitting procedure are shown in Table 2 and reflect trends similar to the ones observed for the Cd–S bonds. For the mean Cd–Cd distances the same dependence on the stabilizing ligand is seen. Again, the mean distances of the polyphosphate-stabilized samples are shortened whereas the 1-thioglycerol-stabilized sample shows an increased mean Cd–Cd distance with respect to CdS bulk. The Debye temperature $T_D = 160(5) \text{ K}$ of the Cd–Cd shell determined by EXAFS is constant in the investigated particle diameter range and is therefore not included in Table 2. It should be noted that it is reduced by a factor of almost 3 with respect to the Cd–S Debye temperature. This means that distance variations between neighboring Cd atoms are much more pronounced compared to vibrations within the Cd–S bonds.³⁹ Thermally induced bond angle variations within the $\text{Cd}_4\text{–S}$ tetrahedron with preferentially unchanged Cd–S bond length would ideally match this observation. In Figure 3, the very different Cd–S and Cd–Cd Debye temperatures are easily recognized in the data by the relatively weak damping of the Cd–S peak in the Fourier transforms but the dramatic effect of temperature on the Cd–Cd peak. Finally, static MSRD and the anharmonicity parameter for the Cd–Cd shell in Table 2 show an overall increase with decreasing particle diameter.

As already mentioned, even at 5 K the Cd–Cd coordination can only be observed for samples with more than 30 Å diameter. Smaller nanoparticles show no significant Cd–Cd shell. This observation is not expected from SC-XRD results of samples 2 and 3. From the known structure of the cluster units in these samples, mean Cd–Cd coordination numbers of 5.88 and 6.75 are obtained. In Figure 9, the experimentally determined Cd–Cd coordination numbers together with the theoretical values for tetrahedra and icosahedra are displayed as a function of particle diameter. The theoretical coordination numbers have been calculated from a formula given by Fritzsche et al.⁴⁰ for a densest packing of spheres. In this description, they depend on the number of atoms on a polyeder edge. To correlate the length of this polyeder edge with the particle diameter given in Figure 9, the diameter of a sphere which incorporates the tetrahedron or icosahedron was used. It is obvious that the coordination number determined by EXAFS is significantly

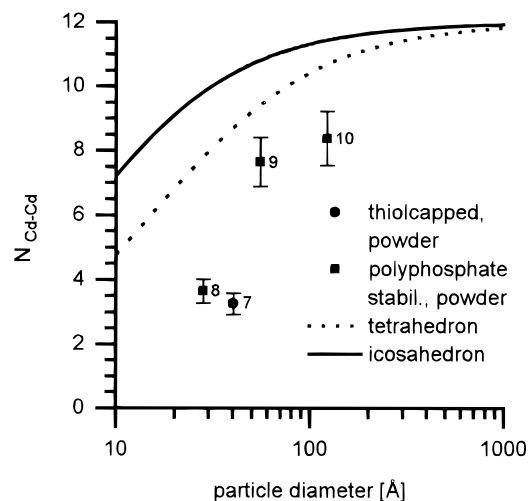


Figure 9. Comparison of the size-dependent change of the Cd–Cd coordination number in CdS nanoparticles determined by EXAFS (symbols) with expected values for particles with ideal icosahedral and tetrahedral shape (lines).

lowered even with regard to an estimated error of 10% and an existing cluster size distribution.

4. Discussion

4.1. Particle Diameter Determination. A critical point in the evaluation of size-dependent structural changes of nanoparticles is the determination of the particle diameter itself. In principle, several methods are available which can determine the particle dimensions in a size range from 10 to several 100 Å. This includes for instance small-angle X-ray scattering, powder X-ray diffraction using particle interference peaks and analyzing the peak broadening in the wide-angle X-ray diffraction regime, and transmission electron microscopy. Also, the EXAFS method has been used by connecting geometrical arguments with the observed size-dependent change in coordination numbers.^{22,24,40–43}

Due to their different principles these methods are sensitive to different size dimensions and each has some limitations. For instance, TEM measurements are sensitive only to CdS nanoparticles larger than 20 Å diameter which may lead to serious misinterpretations of particle size distributions. Furthermore, it is questionable whether the few nanoparticles usually seen in a TEM image are really representative for the whole macroscopic sample. In contrast, powder X-ray diffraction gives a mean particle size in a macroscopic sample, but despite the peak broadening due to the finite crystal size strain in small particles also contributes to this effect. Neglecting this contribution can give particle dimensions which are too small. For instance, from the size quantization effect it is expected that sample 8 with a smaller band gap than sample 7 has a larger particle diameter. In contrast, analyzing the peak broadening in the wide-angle X-ray diffraction regime by the Debye–Scherrer formula gives a diameter which is significantly lower than the particle diameter of sample 7. Since it is known from TEM investigations that the preparation of samples similar to sample 8 yields generally particles with 40 Å diameter,²⁷ the peak broadening of the diffraction peaks is obviously not always suitable for particle size determination. Strain not accounted for or defects in the nanocrystals are the most plausible explanation for this discrepancy.

In literature, several methods are described to deduce information about size and strain in small particles by analyzing the peak broadening of diffraction peaks in the wide-angle X-ray diffraction range.⁴⁴ In this study, no detailed analysis of the

peak broadening has been performed and the Debye–Scherrer equation with a form factor $K = 1$ has been used to determine a rough and mean particle diameter. Since, in principle, this form factor can have values between 0.8 and 1.2 and since it depends on crystal shape and the respective (hkl) reflection, mean particle diameters determined in this way and listed in Table 1 can have an error of up to 20%. Therefore, the good agreement of the particle diameter of sample 7 determined from the particle interference peak in the small angle and the peak broadening in the wide-angle diffraction regime is quite remarkable.

The particle diameter of sample 9 derived from transmission electron microscopy agrees quite well with the Debye–Scherrer results. The somewhat larger differences in the case of samples 8 (see footnote *g* in Table 1) and 10 are probably due to the fact that the preparation method used to synthesize these particles tends to give more polydisperse samples with disordered crystal structures and shapes in this size range. Therefore, our simple analysis of the peak broadening in powder X-ray diffraction patterns which is sensitive to the number of unit cells which scatter the X-ray radiation coherently will systematically underestimate the particle diameter.

Analyzing the diffraction peak in the small-angle regime ($2.0^\circ \leq 2\Theta \leq 10.0^\circ$) as a Bragg peak of lattice planes whose distance is used as an estimate of particle size (see chapter 3.1) needs some further remarks. In ref 9, the size of CdS nanoparticles comparable to sample 6 and 7 in our study have been determined by TEM and the small-angle diffraction peak. A comparison shows that particle diameters determined by the latter one which should be equivalent to distances between the cluster's center are slightly smaller than sizes deduced from TEM. This seems paradoxical since in the powder diffraction measurements the ligand shell of the nanoparticles also contributes to the interparticle spacing, which should therefore be certainly larger than the particle diameter determined by TEM. Without taking into account that TEM especially in this particle size range (20–40 Å diameter) tends to give too large particle diameters, the comparison of these two results shows that the simple identification of the lattice plane distance of the small-angle diffraction peak as particle diameter can be misleading. Nevertheless, the observed discrepancy between the results of TEM and the analysis of the small-angle diffraction peak in ref 9 can be explained by simple geometric arguments. Assuming that the local densest packing of nanoparticles has hexagonal symmetry in a plane perpendicular to the reflecting lattice planes, the particle diameter D_{particle} can be calculated from the lattice plane distance $d_{2\Theta}$ of the respective small-angle diffraction peak by the following equation:

$$D_{\text{particle}} = d_{2\Theta} / \cos 30^\circ$$

In this picture, particle diameters are 15% larger than the lattice plane distance of the small-angle diffraction peak. Taking this into account a good agreement with TEM results in ref 9 can be achieved. Since this analysis requires detailed knowledge of the local structure surrounding a nanoparticle, we omitted this correction of the lattice plane distance and state that particle diameters derived from the small-angle diffraction peak listed in Table 1 may have an error up to 15%. In the crystalline clusters 2 and 3 where the entire structure of the cluster unit is known from SC-XRD, characteristic cluster dimensions are the edge length of the tetrahedron, its height, or the diameter of a sphere which encompasses all the cluster atoms. As seen from Table 1, the latter one agrees well with particle diameters determined from the particle interference peak between $2.0^\circ \leq 2\Theta \leq 10.0^\circ$ using the Bragg equation. Also, the diameter of a

TABLE 3: Comparison of the Mean Cd–S Distance $R_{\text{Cd-S}}$ and the Static MSRD σ_{stat}^2 Determined by EXAFS and SC-XRD for the Crystalline Nanoparticles (Samples 1–3) and Hexagonal CdS Bulk^a

sample	size (Å)	EXAFS	SC-XRD	EXAFS	SC-XRD
		$R_{\text{Cd-S}}$ (5 K) (Å)	$R_{\text{Cd-S}}$ (290 K) (Å)	σ_{stat}^2 (10^{-3} Å^2)	σ_{stat}^2 (10^{-3} Å^2)
1	13.2	2.540	2.534	1.31	1.32
2	13.3	2.537	2.532	0.70	0.99
3	17.5	2.525	2.517	0.73	0.48
11	∞	2.521	2.527	0.00	0.00

^a The EXAFS distances have been scaled to reproduce the mean Cd–S distance of pressed CdS bulk determined by powder X-ray diffraction at room temperature which has been corrected for the thermal contraction of the lattice between 290 and 5 K. The static MSRDs have been calculated for the crystals from the intracenter bond length distribution obtained from the atom lattice positions within a cluster. Errors in the EXAFS results for distances and static MSRDs are $\pm 0.003 \text{ Å}$ and $\pm 0.2 \times 10^{-3} \text{ Å}^2$, respectively.

flat cylinder which envelopes a $\text{Cd}_8(\text{SCH}_2\text{CH}(\text{OH})\text{CH}_2\text{OH})_{16}$ unit agrees well with the dimension determined from the small-angle interference peak. This result suggests that particle diameters of the other samples determined in this way are also a meaningful estimation of a characteristic dimension of the particle. Although we use this small-angle diffraction peak as a simple size determination method which at least works well in our series of quite similar CdS nanoparticles, we want to point out that this small-angle diffraction peak is a rather complex feature which needs a careful interpretation.

Despite the fact that the different methods of size determination are sensitive to different particle dimensions in this study, we used the average in cases where several diameters from different methods were available.

4.2. Cd–S Shell. Samples 1–3 allow a direct comparison of the results obtained by the EXAFS data analysis with the long-range order structure measured by SC-XRD. Since thermally induced bond length variations at 5 K are negligible, these EXAFS data are the most reliable ones to compare with the SC-XRD results. Table 3 lists mean Cd–S bond distances $R_{\text{Cd-S}}$ and static MSRDs σ_{stat}^2 obtained by both methods. It should be noted that the SC-XRD of samples 1–3 have been performed at room temperature and that samples 2 and 3 were measured as single crystals incorporated in a capillary containing several microliters of mother liquor. In contrast, the EXAFS measurements were performed on pressed powders at 5 K. The mean Cd–S bond length in the EXAFS reference compound (sample 11, hexagonal CdS bulk) at 5 K is lowered with respect to the room temperature SC-XRD value⁴⁵ because of the thermal expansion (0.003 Å) and an effect of pressing on the lattice constants (0.004 Å).⁴⁶ The mean Cd–S distances determined by both methods agree in the cluster samples 1–3 within 0.008 Å (see Table 3). However, the 5 K EXAFS values are expected to lie lower than the room temperature SC-XRD values which is not seen in Table 3. In this respect it is pointed out that both techniques are different not only as they measure local versus long-range order structure but also as the distance averages listed in Table 3 are performed in a different manner. For SC-XRD, the mean value over all different Cd–S bond lengths in the cluster calculated from the atomic lattice positions is given. On the other hand, EXAFS weights each Cd–S distance according to the EXAFS formula with its particular Debye–Waller factor, mean-free path damping factor, etc. Furthermore, recently it has been mentioned by Stern et al. that mean distances determined in the usual EXAFS data analysis are slightly larger than crystallographic distances due to vibrations of the neighbor atoms perpendicular to the bond direction.⁴⁷ Considering these

facts and noticing that the full width at half-maximum of the intracuster Cd–S bond length distribution determined by SC-XRD in the cluster samples 1–3 is at least 0.06 Å, the agreement of mean distances in Table 3 is satisfactory.

The values of the static MSR σ^2_{stat} in Table 3 measured by EXAFS and SC-XRD are in good agreement within the estimated error. The result for SC-XRD has been calculated as the variance of the intracuster Cd–S bond length distribution using the equilibrium lattice positions of the atoms. It reflects the inherent distribution of bond distances present in the clusters even in a perfect three-dimensional superlattice. The observed agreement of these values with the EXAFS results in Table 3 is therefore remarkable since it demonstrates that disorder in the superlattice, i.e., the local deviation of the clusters from the average over the whole cluster ensemble in the superlattice, has negligible effect on the actual intracuster Cd–S bond length distribution. The slightly increased EXAFS value of sample 3 which is just within the error bar could be an indication of the latter type of disorder.

The observation of size-dependent shifts of structural parameters determined by EXAFS (Figures 5–8) are in the case of the thiol-stabilized nanoparticles likely to be due to the increasing contribution of their thiol surface. This was already indicated by the ability to describe the data in Figures 6–8 with surface-to-volume dependent functions. In contrast, such a simple picture usually cannot be applied to the small size range: the static MSR σ^2_{stat} in Figure 7 as well as the size dependence of the mean Cd–S distance of the thiol-capped nanoparticles in Figure 5 does not follow a simple surface-to-volume dependent function. As discussed further below, the quite steep increase of the Cd–S bond length in Figure 5 in the smallest samples is instead likely to be caused by additional steric interactions between the thiol ligands. Furthermore, it can be seen from Figure 5 that the Cd–S distance enlargement with decreasing particle diameter depends on the nanocluster's lattice type. The thiol-capped samples 2–5 consist of cubic nanoparticles, whereas samples 6 and 7 according to the C_3 dependence (Figure 8) and powder X-ray diffraction (Figure 2) have the hexagonal wurtzite structure. Correspondingly, the mean Cd–S distances in these samples (6 and 7) show an offset with respect to the cubic thiol-capped samples (2–5) which is equivalent to the distance difference between hexagonal and cubic CdS bulk (0.009 Å). A similar behavior was observed for the anharmonicity parameter C_3 (section 3.2).

In contrast to the thiol-stabilized clusters the cubic nanoparticles with polyphosphate as stabilizer show a slight contraction of the mean Cd–S distance with respect to cubic CdS bulk. The main chemical difference between these two series of nanoparticles consists in the way of the interaction between the ligands and the Cd atoms at the surface. In the case of thiol ligands strong covalent bonds between sulfur of the ligands and Cd atoms of the cluster core are formed. With decreasing particle diameter the number of ligands necessary to saturate all Cd atoms at the particle surface increases relative to the total surface area. Below a critical particle diameter the steric requirements for these ligands will be larger than the available space which can be provided by the limited surface area of the nanoparticles. This will lead to serious steric interactions between these ligands and forces the CdS core in the particles to expand to yield more surface area and therefore more space for the ligands. On the other hand, the polyphosphate ligands are thought to coordinate in a more ionic way. Furthermore, from stoichiometry it is not expected that every Cd atom at the surface is bound to an oxygen from the ligand. These two effects lead to the idea that in the polyphosphate-stabilized

nanoparticles the CdS core has no strong interaction with the ligand shell. This will allow a contraction of the CdS core in the polyphosphate-stabilized nanoparticles like a liquid droplet which tries to minimize its surface as a consequence of its surface tension, which seems to be prevented by the thiol ligands in samples 1–7. Additionally, the idea that at the surface of polyphosphate-stabilized nanoparticles cadmium ions with their reduced radius compared to covalently bound cadmium atoms are present is consistent with the observed reduced mean Cd–S distance in polyphosphate-stabilized CdS nanoparticles. Solid state EXAFS studies of CdX (X = S, Se, Te) nanoparticles^{19,20} in a similar size range state that they observe no change or a slight contraction of the Cd–X first shell mean distance which is smaller than 0.03 Å with respect to bulk material. This could be a result of a simplified data analysis not taking into account the anharmonicity of the Cd–X pair distribution function and therefore neglecting anharmonic contributions in the interatomic potential which can lead to reduced interatomic distances.^{43,48} To our knowledge, we observed in our EXAFS study for the first time a systematic expansion of interatomic mean distances of cadmium chalcogenide nanoparticles with decreasing particle diameter.

The slight decrease of vibrational amplitudes of the nearest neighbor bond with decreasing particle diameter has also been observed to different extents in other studies.^{16,20} We performed no detailed analysis since the effect is in our case rather small, within 5%.

A quite common observation is that nanoparticles have an enlarged static MSR σ^2_{stat} with respect to bulk material. This is also true in our crystalline samples 1–3 although they appear to be more ordered than the nanocrystalline samples 4–10. The size-dependent increase of the static MSR σ^2_{stat} of samples 6–10 can be explained by the changing surface-to-volume ratio. From Figure 7 it is seen that there seems to be a transition in the static MSR σ^2_{stat} around particles with 20–40 Å diameter. Apparently in our series of CdS nanoclusters, this transition regime separates the range of the thermodynamically controlled cluster growth leading to small defined clusters with distinct absorption maxima from the colloidal range where nanoparticle growth mainly proceeds via Ostwald ripening. The thermodynamic control of cluster growth obviously leads to particles with reduced static MSR σ^2_{stat} s, which is a prerequisite for crystallization of these particles into three-dimensional superlattices. Only in sample 1 which models the cluster surface does the intrinsic width of the intracuster Cd–S bond length distribution in single crystals cause again an increased static MSR σ^2_{stat} . As described in the discussion of Table 3, the observed static MSR σ^2_{stat} in the nanocrystalline samples is not disorder in a crystallographic sense but the consequence of the surface-induced bond length distribution. From the good agreement between samples of similar diameter but different ligands and long-range order, it can be concluded that the type of ligand has only a slight influence on the static MSR σ^2_{stat} in the clusters. The ligand seems to determine whether the nanoparticles can crystallize in a three-dimensional superlattice or not. Therefore, surface reconstructions or defects which induce strain in the cluster core are the most probable explanations for the observed increased static MSR σ^2_{stat} in the intermediate size range.

The anharmonicity parameter C_3 in Figure 8 shows quite interesting differences between samples 6 and 7 and all others. The structure of the latter ones, corresponding to powder X-ray diffraction or SC-XRD, is a cutout of the zinc blende lattice whereas sample 7 shows a powder X-ray diffraction pattern of the wurtzite lattice. The difference in the first shell surrounding

a Cd atom between hexagonal and cubic bulk CdS is, despite different absolute bond distances, the more symmetrical arrangement of the four sulfur atoms in the cubic case. Here, all four sulfurs have the same distance of 2.515 Å to the central Cd atom (at room temperature), whereas in our pressed hexagonal bulk (sample 11) there are three Cd–S distances of 2.521 Å and one of 2.532 Å. This obviously leads to an increased anharmonicity in the interatomic potential in the hexagonal lattice which can be detected by the anharmonicity parameter C_3 in the EXAFS data analysis. This point is seen in Figure 8 since the size dependence of the cubic samples approaches a value of zero for a cubic CdS bulk⁴⁹ whereas an enlarged anharmonicity for the hexagonal bulk is observed. The experimentally observed value for hexagonal bulk is too large in comparison to the calculated value of C_3 according to the bond length differences determined by SC-XRD. However, one has to consider that EXAFS measures local static and, even at 5 K, additional contributions to C_3 due to zero-point vibrations. Figure 8 therefore strongly indicates that samples 6 and 7 with increased C_3 values with respect to cubic samples of similar diameter and the hexagonal CdS bulk have hexagonal lattices. In contrast, all other samples with a smaller C_3 correspond to cubic lattices. With regard to the preparation of samples 6 and 7 at higher temperatures in boiling dimethylformamide (bp 153 °C), the assignment of a hexagonal lattice supports the idea that at higher temperatures the formation of the thermodynamic more stable hexagonal lattice is favored even in these clusters. The increasing anharmonicity in both series of C_3 in Figure 8 with decreasing particle diameters is most likely due to the strong asymmetric interatomic potential at the nanoparticle's surface. It should be noticed that, although SC-XRD on the crystalline cluster samples 2 and 3 shows an essentially cubic lattice of the tetrahedral nanoparticles, the four corners of each tetrahedron consists of (CdS)₃ rings in a boat conformation which reflects the structure unit in hexagonal CdS bulk along the *c*-axis. Assuming a tetrahedral shape for the thiol-capped nanoparticles, this geometry would give a size-independent contribution to the anharmonicity. The increase in C_3 between samples 2 and 3 with known tetrahedral particle shape, however, cannot be explained in this manner. Probably, this effect can also be neglected for other samples in comparison to the majority surface contribution with the chair conformation.

4.3. Cd–Cd Shell. The trends in Table 2 observed for mean Cd–Cd distances, Debye temperatures, static MSRD, and third moment of the Cd–Cd pair distribution function are similar to the ones determined for the Cd–S bonds.

In contrast, mean Cd–Cd coordination numbers obtained from the EXAFS fits are strongly reduced in small particles and no second coordination shell is observed in particles smaller than 30 Å. This result is consistent with other studies on CdX (X = S, Se, Te) nanoparticles.^{19,20} In the smaller clusters the vanishing Cd–Cd coordination shell could be explained by sufficiently large static bond distance fluctuations, i.e., non-equivalent clusters in the sample. However, Figure 9 shows that this explanation is doubtful for larger nanoclusters with nonvanishing Cd–Cd contributions. For the latter samples, mean Cd–Cd coordination numbers are determined from the EXAFS fits which are considerably reduced with respect to values calculated for simple cluster geometries like tetrahedra and icosahedra.⁴⁰ On the other hand, the static MSRD of the Cd–Cd shell extracted from EXAFS data (see Table 2) is not enhanced to an extent that it would smear out the Cd–Cd coordination shell significantly. Of course, much more open cluster geometries would explain the result of Figure 9. However, it is tempting to postulate a mechanism for the

reduction of the higher coordination shells in small as well as large nanoparticles. For example, it was shown in calculations that using the mean free path (MFP) of the photoelectron in aluminum bulk yields an underestimation of the first shell coordination number in 20 Å Al particles by 25%.⁵⁰ A more detailed discussion of the analysis of the Cd–Cd shell will be presented in a forthcoming publication.⁵¹

5. Summary and Conclusions

EXAFS analysis on CdS nanoparticles with 13–120 Å diameter revealed that the stabilization of the nanoparticles clearly influences the mean Cd–S distance. Thiol-capped nanoparticles exhibit an expansion of their interatomic mean Cd–S distance, whereas polyphosphate-stabilized particles are slightly contracted with respect to CdS bulk. This opposite behavior is most likely due to steric interactions between the ligands in the case of stabilization by thiols whereas in polyphosphate-stabilized samples no hindering is given to prevent the contraction of the nanoparticle to minimize its surface energy. A strong dependence of the X-ray absorption spectra on temperature was observed. Especially, the second coordination shell is extremely sensitive to temperature-dependent displacements of atoms, resulting in damped oscillations even in CdS bulk at 50 K. This observation suggests that for a detailed understanding of the structure of nanoparticles low-temperature measurements preferably at 5 K are essential. As shown, such temperature variations also allow separation of static and temperature-dependent contributions to the mean-square relative displacements. The static MSRD is increased for all nanoparticles and shows a maximum around 30 Å particle diameter which separates the regime of thermodynamically governed cluster growth leading to molecular crystals of CdS nanoparticles from the colloidal regime where particle growth proceeds via Ostwald ripening. On the other hand, with decreasing particle size the vibrational amplitude of the Cd–S bond is only very slightly reduced. An interesting possibility to gain information about “long-range order” within nanoparticles based on the analysis of the anharmonicity of the Cd–S pair potential has been presented. EXAFS in contrast to SC-XRD is only sensitive to the local geometrical arrangement of neighboring atoms surrounding the absorbing atom. In this study, it is shown that the anharmonicity of the interatomic Cd–S pair potential is sensitive to the crystal lattice type within the nanoclusters, thereby linking short- and long-range order measurements. Samples with the zinc blende structure show a smaller value of the anharmonicity parameter C_3 than CdS bulk and nanoparticles with the wurtzite lattice. This method can therefore be used to determine the lattice of nanoparticles where powder X-ray diffraction (due to the very broad diffraction patterns) or TEM (due to the vanishing contrast in very small particles) fails. Preliminary measurements on nanoparticles in aqueous solution at room temperature show results very similar to those in the solid state. Especially, the mean Cd–S distance is also enlarged with regard to cubic CdS bulk.

Acknowledgment. We thank L. Katsikas, H. Meyssamy, S. Naused, and A. L. Rogach for their help in the preparation of the samples and valuable discussions. TEM measurements have been performed by D. Su and U. Bloeck, Hahn-Meitner-Institut, Berlin. G. Klaska from the Mineralogisch-Petrographisches Institut, Universität Hamburg, provided the powder X-ray diffraction data. Helpful discussions with G. Reck, Bundesanstalt für Materialprüfung, Berlin, are gratefully acknowledged. Financial support was provided by the Deutsche Forschungsgemeinschaft.

References and Notes

- (1) Henglein, A. *Chem. Rev.* **1989**, 89, 1861.
- (2) Weller, H. *Angew. Chem., Int. Ed. Engl.* **1993**, 32, 41.
- (3) Alivisatos, A. P. *J. Phys. Chem.* **1996**, 100, 13226.
- (4) Brus, L. J. *Chem. Phys.* **1984**, 80, 4403.
- (5) Lee, G. S. H.; Craig, D. C.; Ma, I.; Scudder, M. L.; Bailey, T. D.; Dance, I. G. *J. Am. Chem. Soc.* **1988**, 110, 4863.
- (6) Herron, N.; Calabrese, J. C.; Farneth, W. E.; Wang, Y. *Science* **1993**, 259, 1426.
- (7) Vossmeier, T.; Reck, G.; Katsikas, L.; Haupt, E. T. K.; Schulz, B.; Weller, H. *Science* **1995**, 267, 1476.
- (8) Vossmeier, T.; Reck, G.; Schulz, B.; Katsikas, L.; Weller, H. *J. Am. Chem. Soc.* **1995**, 117, 12881.
- (9) Vossmeier, T.; Katsikas, L.; Giersig, M.; Popovic, I. G.; Diesner, K.; Chemseddine, A.; Eychmüller, A.; Weller, H. *J. Phys. Chem.* **1994**, 98, 7665.
- (10) Murray, C. B.; Kagan, C. R.; Bawendi, M. G. *Science* **1995**, 270, 1335.
- (11) Kakar, S.; Björneholm, O.; Weigelt, J.; de Castro, A. R. B.; Tröger, L.; Frahm, R.; Möller, T.; Knop, A.; Rühl, E. *Phys. Rev. Lett.*, accepted for publication.
- (12) Schmid, G.; Pfeil, R.; Boese, R.; Bandermann, F.; Meyer, S.; Calis, G. H. M.; van der Velden, J. W. A. *Chem. Ber.* **1981**, 114, 3634.
- (13) Schmid, G. *Polyhedron* **1988**, 7, 2321.
- (14) Schmid, G.; Harms, M.; Malm, J. O.; Bovin, J. O.; van Ruitenbeek, J.; Zandbergen, H. W.; Fu, W. T. *J. Am. Chem. Soc.* **1993**, 115, 2046.
- (15) Cluskey, P. D.; Newport, R. J.; Benfield, R. E.; Gurman, S. J.; Schmid, G. *Phys. D* **1993**, 26, S 8.
- (16) Marcus, M. A.; Andrews, M. P.; Zegenhagen, J.; Bommanavar, A. S.; Montano, P. *Phys. Rev. B* **1990**, 42, 3312.
- (17) Benfield, R. E.; Filipponi, A.; Bowron, D. T.; Newport, R. J.; Gurman, S. J.; Schmid, G. *Physica B* **1995**, 208–209, 671.
- (18) Moller, K.; Eddy, M. M.; Stucky, G. D.; Herron, N.; Bein, T. *J. Am. Chem. Soc.* **1989**, 111, 2564.
- (19) Marcus, M. A.; Flood, W.; Steigerwald, M.; Brus, L.; Bawendi, M. *J. Phys. Chem.* **1991**, 95, 1572.
- (20) Marcus, M. A.; Brus, L. E.; Murray, C.; Bawendi, M. G.; Prasad, A.; Alivisatos, A. P. *Nanostruct. Mater.* **1992**, 1, 323.
- (21) Hosokawa, H.; Fujiwara, H.; Murakoshi, K.; Wada, Y.; Yanagida, S.; Satoh, M. *J. Phys. Chem.* **1996**, 100, 6649.
- (22) Ashcroft, A. T.; Cheetham, A. K.; Harris, P. J. F.; Jones, R. H.; Natarajan, S.; Sankar, G.; Stedman, N. J.; Thomas, J. M. *Catal. Lett.* **1994**, 24, 47.
- (23) Clausen, B. S.; Gråbæk, L.; Steffensen, G.; Hansen, P. L.; Topsøe, H. *Catal. Lett.* **1993**, 20, 23.
- (24) Kip, B. J.; Duivenvoorden, F. B. M.; Koningsberger, D. C.; Prins, R. *J. Catal.* **1987**, 105, 26.
- (25) Vossmeier, T.; Reck, G.; Katsikas, L.; Haupt, E. T. K.; Schulz, B.; Weller, H. *Inorg. Chem.* **1995**, 34, 4926.
- (26) Chemseddine, A.; Weller, H. *Ber. Bunsen-Ges. Phys. Chem.* **1993**, 97, 636.
- (27) Spanhel, L.; Haase, M.; Weller, H.; Henglein, A. *J. Am. Chem. Soc.* **1987**, 109, 5649.
- (28) Haase, M.; Alivisatos, A. P. *J. Phys. Chem.* **1992**, 96, 6756.
- (29) Tolbert, S. H.; Alivisatos, A. P. *J. Phys. Chem.* **1995**, 102, 4642.
- (30) Prins, R.; Koningsberger, D. C. *X-Ray Absorption. Principles, Applications, Techniques of EXAFS, SEXAFS and XANES*, 1st ed.; Wiley: New York, 1988.
- (31) Stern, E. A.; Newville, M.; Ravel, B.; Yacoby, Y.; Haskell, D. *Physica B* **1995**, 208–209, 117.
- (32) Rehr, J. J.; Albers, R. C.; Zabinsky, S. I. *Phys. Rev. Lett.* **1992**, 69, 3397.
- (33) Young, R. A.; Sakthivel, A.; Moss, T. S.; Paiva-Santos, C. O. *User's Guide to Program DBWS-9411*; 30.3.95; School of Physics, Georgia Institute of Technology, Atlanta.
- (34) JCPDS 6-314 and 10-454, 1989.
- (35) Vaarkamp, M.; Dring, I.; Oldman, R. J.; Stern, E. A.; Koningsberger, D. C. *Phys. Rev. B* **1994**, 50, 7872.
- (36) Li, G. G.; Bridges, F.; Booth, C. H. *Phys. Rev. B* **1995**, 52, 6332.
- (37) A Cd–S bond length expansion of 0.003 Å between 5 and 290 K calculated from the bulk thermal expansion was taken into account.
- (38) Traill, B. *Am. Mineral.* **1955**, 40, 555.
- (39) More precisely, EXAFS measures predominantly the projection of the thermal vibrations along the bond direction.
- (40) Fritsche, H. G.; Benfield, R. E. *Z. Phys. D* **1993**, 26, S 15.
- (41) Gregor, R. B.; Lytle, F. W. *J. Catal.* **1980**, 63, 476.
- (42) Montano, P. A.; Zhao, J.; Ramanathan, M.; Shenoy, G. K.; Schulze, W.; Urban, J. *Chem. Phys. Lett.* **1989**, 164, 126.
- (43) Clausen, B. S.; Gråbæk, L.; Topsøe, H.; Hansen, L. B.; Stoltze, P.; Nørskov, J. K.; Nielsen, O. H. *J. Catal.* **1993**, 141, 368.
- (44) Klug, H. P.; Alexander, L. E. *X-Ray Diffraction Procedures*, 2nd ed.; J. Wiley & Sons: New York, 1974.
- (45) Stevenson, A. W.; Milanko, M.; Barnea, Z. *Acta Crystallogr. B* **1984**, 40, 521.
- (46) This was verified by X-ray diffraction at room temperature. The derived lattice constants for the original hexagonal CdS powder agree with literature within 0.001 Å (ref 45), whereas the pressed samples show slightly lowered parameters.
- (47) Stern, E. A. *J. Phys. (Coll.)* Proceedings of the XAFS IX conference, Grenoble 1996.
- (48) Hansen, L. B.; Stoltze, P.; Nørskov, J. K.; Clausen, B. S.; Niemann, W. *Phys. Rev. Lett.* **1990**, 64, 3155.
- (49) This is consistent with the observation that a similar EXAFS data analysis as presented in this study on Cd K edge spectra of cubic CdTe bulk at 8 K shows in comparison to hexagonal CdS bulk a significantly reduced anharmonicity of the interatomic potential.
- (50) Zhao, J.; Montano, P. A. *Phys. Rev. B* **1989**, 40, 3401.
- (51) Tröger, L.; Rockenberger, J.; Kornowski, A.; Eychmüller, A.; Weller, H. Manuscript in preparation.